First-Principles Calculations of Stability, Electronic Structure, and Mechanical Properties of *M* (Mn, Ti, Mo)-Doped α-Fe*

Hua Sunmingqiang[1], Kong Detong[1], Hu Xiao[1], She Xu[1], Wang Xiao[2], Wang Yuan[1, 3]

1. School of Mechanical and Transportation Engineering, Southwest Forestry University, Kunming 650224
2. City College, Kunming University of Science and Technology, Kunming 650051
3. Yunnan Key Laboratory of Forest Disaster Early Warning and Control, Kunming 650224

Abstract

Ferrite (α-Fe), as a fundamental phase of steel materials, plays a decisive role in determining their macroscopic mechanical behaviors through its microscopic properties, particularly in engineering applications involving resistance to plastic deformation and fracture, fatigue resistance, wear resistance, and low-temperature toughness. Therefore, alloying elements are commonly introduced to improve the performance of steel via mechanisms such as grain refinement strengthening and precipitation strengthening. However, in these strengthening mechanisms, the effects of doped alloying elements on the stability, electronic structure, and mechanical properties of ferrite itself have not been thoroughly investigated. In this study, orthogonal experimental design and first-principles calculations are employed to investigate the effects of ternary alloy doping with *M* (Mn, Ti, Mo) on the stabilities, electronic structures, and mechanical properties of a ferrite-based supercell model $Fe_{16-x-y-z}Mn_xTi_yMo_z$ (x, y, or z = 0, 1, or 2), aiming to provide both theoretical insight and experimental reference for improving the comprehensive performance of ferrite-based steels by modifying the properties of the matrix phase. The results of the formation enthalpy (H_{form}) calculations indicate that all solid solutions have negative formation enthalpies, suggesting that they can form spontaneously. Among them, Ti doping is the most favorable for solid solution formation, followed by Mn, with Mo being the least favorable. The $Fe_{13}Ti_1Mo_2$ configuration is the easiest to form spontaneously. The cohesive energy (E_{coh}) results demonstrate that all solid solutions exhibit structural stabilities. $Fe_{13}Ti_1Mo_2$ has the largest (most negative) cohesive energy of –477.96 eV, indicating that it possesses the highest structural stability. The

---

* The paper is an English translated version of the original Chinese paper published in Acta Physica Sinica. Please cite the paper as: Hua Sunmingqiang[1], Kong Detong[1], Hu Xiao[1], She Xu[1], Wang Xiao[2], Wang Yuan[1, 3], **First-Principles Calculations of Stability, Electronic Structure, and Mechanical Properties of *M* (Mn, Ti, Mo)-Doped α-Fe.** *Acta Phys. Sin.*, 2025, 74(4): 246202. DOI: 10.7498/aps.74.20251044

contribution of Mo doping to stability enhancement is the greatest, followed by Ti, while the influence of Mn is the smallest. Electronic structure calculations reveal that M doping consistently reduces the density of states (DOS) at the Fermi level for $Fe_{16-x-y-z}Mn_xTi_yMo_z$. The lowest DOS at the Fermi level is found to be 4.294 in $Fe_{13}Ti_1Mo_2$, indicating enhanced hybridization and overlap between Mn 3d, Ti 3d, Mo 4d, and Fe 3d states. This strong hybridization leads to a decrease in the Fermi level and contributes to the high stability of the $Fe_{13}Ti_1Mo_2$ phase. Mechanical property calculations indicate that M doping reduces the Young's modulus (E) and Vickers hardness (H_V) of the solid solutions. However, the K values ($K = G_H/B_H$) are all greater than 1.75, and Poisson's ratios (v) exceed 0.26, implying that while stiffness and hardness decrease, the ductility of the materials is improved. This study provides valuable guidance for designing ductile and tough ferrite-based steel materials.

Ferrite (α-Fe), as a fundamental phase of steel materials, plays a decisive role in determining their macroscopic mechanical behaviors through its microscopic properties, particularly in engineering applications involving resistance to plastic deformation and fracture, fatigue resistance, wear resistance, and low-temperature toughness. Therefore, alloying elements are commonly introduced to improve the performance of steel via mechanisms such as grain refinement strengthening and precipitation strengthening. However, in these strengthening mechanisms, the effects of doped alloying elements on the stability, electronic structure, and mechanical properties of ferrite itself have not been thoroughly investigated. In this study, orthogonal experimental design and first-principles calculations are employed to investigate the effects of ternary alloy doping with M (Mn, Ti, Mo) on the stabilities, electronic structures, and mechanical properties of a ferrite-based supercell model $Fe_{16-x-y-z}Mn_xTi_yMo_z$ (x, y, or z = 0, 1, or 2), aiming to provide both theoretical insight and experimental reference for improving the comprehensive performance of ferrite-based steels by modifying the properties of the matrix phase. The results of the formation enthalpy (H_{form}) calculations indicate that all solid solutions have negative formation enthalpies, suggesting that they can form spontaneously. Among them, Ti doping is the most favorable for solid solution formation, followed by Mn, with Mo being the least favorable. The $Fe_{13}Ti_1Mo_2$ configuration is the easiest to form spontaneously. The cohesive energy (E_{coh}) results demonstrate that all solid solutions exhibit structural stabilities. $Fe_{13}Ti_1Mo_2$ has the largest (most negative) cohesive energy of –477.96 eV, indicating that it possesses the highest structural stability. The contribution of Mo doping to stability enhancement is the greatest, followed by Ti, while the influence of Mn is the smallest. Electronic structure calculations reveal that M doping consistently reduces the density of states (DOS) at the Fermi level for $Fe_{16-x-y-z}Mn_xTi_yMo_z$. The lowest DOS at the Fermi level is found to be 4.294 in $Fe_{13}Ti_1Mo_2$, indicating enhanced hybridization and overlap between Mn 3d, Ti 3d, Mo 4d, and Fe 3d states. This strong hybridization leads to a decrease in the Fermi level and contributes to the high stability of the $Fe_{13}Ti_1Mo_2$ phase. Mechanical property calculations indicate that M doping reduces the Young's modulus (E) and Vickers hardness (H_V) of the solid solutions. However, the K values ($K = G_H/B_H$) are all greater than 1.75, and Poisson's ratios (v) exceed 0.26, implying that while stiffness

and hardness decrease, the ductility of the materials is improved. This study provides valuable guidance for designing ductile and tough ferrite-based steel materials.

Keywords： ferrite (α-Fe); Mn; Ti; Mo doping; first-principles; mechanical properties

PACS：62.20.-x; 71.15.Mb
doi: 10.7498/aps.74.20251044
cstr: 32037.14.aps.74.20251044

1 Introduction

Ferrite (α-Fe), as a fundamental phase in steel materials, directly governs their macroscopic mechanical behavior. It exerts a decisive influence on engineering performance, particularly regarding resistance to plastic deformation and fracture, fatigue, wear, and low-temperature toughness[1]. Consequently, alloying elements are commonly introduced into steel to achieve grain refinement and precipitation strengthening. For instance, Ti-Mo co-doping precipitates nanoscale, spherical, and uniformly dispersed Ti-Mo carbonitrides, thereby enhancing the tensile properties of fully ferritic microalloyed high-strength steel[2,3]. Similarly, Ti-Nb co-doping reduces the grain growth tendency in 30% Cr super ferritic stainless steel by approximately 30%, yielding grain refinement that improves room-temperature strength and hardness. However, the brittle inclusions formed during this process degrade low-temperature toughness[4]. Although grain refinement and precipitation strengthening effectively increase strength, they often compromise toughness or elevate the ductile-to-brittle transition temperature. Moreover, existing studies primarily focus on grain size and precipitate types, without elucidating intrinsic changes in ferrite properties.

Currently, first-principles calculations that modulate electronic structures to optimize material performance have emerged as a novel strategy to overcome the strength-toughness trade-off in metals. Examples include first-principles investigations of Cr-doped $CuZr_2$[5], rare-earth element *X*-doped GaSe[6], and Mg-Ti co-doped $LiFePO_4$[7]. Mn, Ti, and Mo are frequently employed as alloying elements to strengthen steel. Mn doping enhances strength via solid-solution strengthening, yet excessive Mn (>2 at.%) induces grain boundary segregation, thereby reducing toughness[8]. Ti doping generates nanoscale precipitates that produce the Orowan effect, increasing peak strength by 300 MPa. Mo doping segregates to grain boundaries, refining precipitates and impeding grain boundary migration to further refine grains[9,10]. Nevertheless, the lattice distortion and relative stability arising from the opposing effects-Mn expanding the α-Fe lattice while Ti/Mo contract it-remain unquantified[11]. Additionally, the evolution of the doping-induced density of states

(DOS) near the Fermi level is still unclear. Furthermore, most prior research addresses single or binary doping systems, leaving a significant knowledge gap regarding the electronic mechanisms underlying the stability and mechanical properties of α-Fe under ternary Mn-Ti-Mo co-doping.

In summary, this study employs first-principles calculations combined with orthogonal experimental design to construct $Fe_{16-x-y-z}Mn_xTi_yMo_z$ (x, y, or z = 0, 1, or 2) supercell models. We systematically investigate the effects of M (Mn, Ti, Mo) doping on stability, electronic structure, and mechanical properties. This work aims to clarify the electronic mechanisms of strength-toughness synergy in ternary co-doped α-Fe and provide a theoretical foundation for designing ferrite-based steels with tailored performance.

2 Computational Methods and Models

α-Fe adopts a body-centered cubic (BCC) crystal structure with space group $Im\bar{3}m$ and lattice parameters $a = b = c = 2.866$ Å. Each unit cell contains two Fe atoms: one at the body center and the other formed by the combined contribution of eight corner atoms, each contributing 1/8 of an atom. To thoroughly examine the influence of M doping on the stability, electronic characteristics, and mechanical properties of α-Fe, we employ a special quasi-random structure (SQS) method[12] to simulate the disordered atomic arrangement in solid solutions, adhering to the principle of energy minimization. To mitigate periodic boundary condition artifacts, we expand the α-Fe unit cell into a 2×2×2 supercell to construct the $Fe_{16-x-y-z}Mn_xTi_yMo_z$ model, as illustrated in Figure 1.

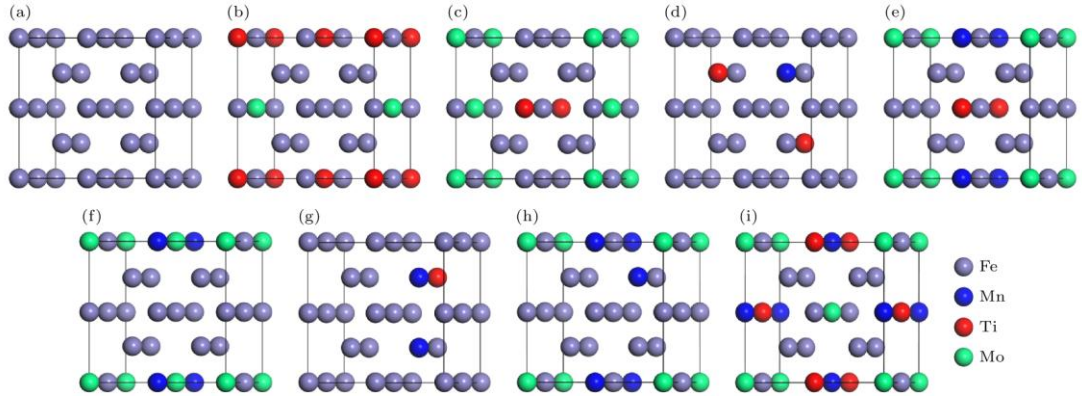

Fig. 1 Supercell model of $Fe_{16-x-y-z}Mn_xTi_yMo_z$: (a) Fe_{16}; (b) $Fe_{13}Ti_2Mo_1$; (c) $Fe_{13}Ti_1Mo_2$; (d) $Fe_{13}Mn_1Ti_2$; (e) $Fe_{13}Mn_1Ti_1Mo_1$; (f) $Fe_{13}Mn_1Mo_2$; (g) $Fe_{13}Mn_2Ti_1$; (h) $Fe_{13}Mn_2Mo_1$; (i) $Fe_{10}Mn_2Ti_2Mo_2$.

All supercells were designed based on the three non-stoichiometric concentrations listed in Table 1, exhibiting a typical BCC structure. An orthogonal experimental design yielded an $L_9(3^3)$ model with three factors and three levels. In the supercells,

the values of *x*, *y*, or *z* (0, 1, or 2) correspond to atomic concentrations of the dopant element *M* of 0, 6.25%, or 12.5%, respectively. Using density functional theory (DFT)[13], we employed the CASTEP module in Materials Studio to calculate the stability, electronic structure, and mechanical properties of $Fe_{16-x-y-z}Mn_xTi_yMo_z$. Norm-conserving pseudopotentials were selected to describe ion-electron interactions, and the BFGS algorithm was used for crystal structure optimization[14]. The exchange-correlation energy was treated within the generalized gradient approximation (GGA) using the Perdew-Burke-Ernzerhof (PBE) functional[15]. Since α-Fe is intrinsically ferromagnetic and all *M* elements are magnetic, spin-polarized calculations combined with LDA+*U* were implemented to correct electronic structures and energies, thereby mitigating the influence of magnetic moments, magnetic ordering, or strong correlations. In the spin-polarized calculations, initial spins for Fe, Mn, Ti, and Mo were set to +4, +5, 0, and +2 μ_B, respectively. To enhance computational accuracy, the *K*-point mesh density in the first Brillouin zone was refined to 8×8×8, with a grid spacing of 0.02/atom. Self-consistent calculations employed the Pulay charge mixing scheme, with a convergence threshold of 1.0×10^{-5} eV/atom for total energy and 1.0×10^{-6} eV/atom for the self-consistent energy loop. Interatomic forces in the model were maintained below 0.03 eV/Å, with displacement tolerance under 1.0×10^{-3} nm and stress tolerance below 0.05 GPa. A ultrasoft pseudopotential described valence electron-ion core interactions, and a plane-wave cutoff energy of 500 eV was determined from self-consistent energy convergence tests. Elastic constants were computed via the stress-strain method using geometrically optimized cells, applying six distinct strain amplitudes per mode, with a maximum amplitude of 0.2%. The dopant *M* randomly substituted Fe atoms in all structures; based on the minimum energy principle, the configuration with the lowest total energy was selected for subsequent analysis. All calculations were performed at 0 GPa and 0 K.

Table 1 Orthogonal experimental design and atomic percentage content of *M*-doped α-Fe.

超胞	元素 *M* 原子百分比/%		
	Mn	Ti	Mo
Fe_{16}	0	0	0
$Fe_{13}Ti_2Mo_1$	0	12.5	6.25
$Fe_{13}Ti_1Mo_2$	0	6.25	12.5
$Fe_{13}Mn_1Ti_2$	6.25	12.5	0
$Fe_{13}Mn_1Ti_1Mo_1$	6.25	6.25	6.25
$Fe_{13}Mn_1Mo_2$	6.25	0	12.5
$Fe_{13}Mn_2Ti_1$	12.5	6.25	0
$Fe_{13}Mn_2Mo_1$	12.5	0	6.25
$Fe_{10}Mn_2Ti_2Mo_2$	12.5	12.5	12.5

3 Results and Discussion

3.1 Structural Stability

Formation enthalpy (H_{form}) represents the energy absorbed or released during a reaction[16]. Lower values indicate that substitutionally doped compounds form more readily. Cohesive energy (E_{coh}) reflects the stability of a compound[17]; a larger absolute value of cohesive energy signifies a more structurally stable compound that is less prone to change. We determined structural stability by calculating the volumetric strain (ε), H_{form}, and E_{coh}, using Equations (1) through (3), respectively:

$$\varepsilon = \frac{V - V_0}{V_0}, \quad (1)$$

$$H_{\text{from}} = \frac{1}{N_{\text{Fe}} + N_{\text{Mn}} + N_{\text{Ti}} + N_{\text{Mo}}} (E_{\text{t}} - N_{\text{Fe}} E_{\text{s}}^{\text{Fe}} - N_{\text{Mn}} E_{\text{s}}^{\text{Mn}} - N_{\text{Ti}} E_{\text{s}}^{\text{Ti}} - N_{\text{Mo}} E_{\text{s}}^{\text{Mo}}), \quad (2)$$

$$E_{\text{coh}} = \frac{1}{N_{\text{Fe}} + N_{\text{Mn}} + N_{\text{Ti}} + N_{\text{Mo}}} (E_{\text{t}} - N_{\text{Fe}} E_{\text{a}}^{\text{Fe}} - N_{\text{Mn}} E_{\text{a}}^{\text{Mn}} - N_{\text{Ti}} E_{\text{a}}^{\text{Ti}} - N_{\text{Mo}} E_{\text{a}}^{\text{Mo}}), \quad (3)$$

In the equation, V_0 denotes the unit cell volume of Fe_{16}, V represents the unit cell volume of $Fe_{16-x-y-z}Mn_xTi_yMo_z$, N is the number of atoms in the unit cell, E_t is the total energy of the compound, E_s is the chemical potential, and E_a is the energy of an isolated atom. Formation energies obtained via DFT calculations can approximate formation enthalpies under specific conditions. Fe and Mo adopt the BCC structure, Mn adopts the FCC structure, and Ti adopts the HCP structure[18-20]. The total energy of isolated atoms was computed by constructing a unit cell containing a single isolated atom, accounting for spin polarization.

As listed in Table 2, the H_{form} values for all solid solutions are negative, indicating their spontaneous formation. Ordered from easiest to most difficult to form, the sequence is: $Fe_{13}Ti_2Mo_1$, $Fe_{13}Mn_1Ti_2$, $Fe_{10}Mn_2Ti_2Mo_2$, $Fe_{13}Ti_1Mo_2$, $Fe_{13}Mn_1Ti_1Mo_1$, $Fe_{13}Mn_2Ti_1$, Fe_{16}, $Fe_{13}Mn_1Mo_2$, and $Fe_{13}Mn_2Mo_1$. Consequently, all solid solutions except $Fe_{13}Mn_1Mo_2$ and $Fe_{13}Mn_2Mo_1$ form preferentially over Fe_{16}.

Table 2 Calculated values of ε, H_{form} and E_{coh} for $Fe_{16-x-y-z}Mn_xTi_yMo_z$.

超胞	晶胞体积/Å^3	ε/%	H_{form}/(kJ·mol^{-1})	E_{coh}/(kJ·mol^{-1})
Fe_{16}	178.79	—	–7.51	–449.39
$Fe_{13}Ti_2Mo_1$	190.51	6.56	–16.52	–477.95
$Fe_{13}Ti_1Mo_2$	190.70	6.66	–10.73	–477.96
$Fe_{13}Mn_1Ti_2$	185.61	3.81	–15.48	–460.85
$Fe_{13}Mn_1Ti_1Mo_1$	187.73	5.00	–10.40	–461.58
$Fe_{13}Mn_1Mo_2$	188.92	5.67	–5.37	–462.35
$Fe_{13}Mn_2Ti_1$	182.89	2.29	–9.53	–444.06
$Fe_{13}Mn_2Mo_1$	184.48	3.18	–4.58	–445.51
$Fe_{10}Mn_2Ti_2Mo_2$	194.98	9.06	–12.97	–473.45

Based on the absolute values of cohesive energy (E_{coh}) listed in Table 2, the stability of the solid solutions, ranked from highest to lowest, is as follows: $Fe_{13}Ti_1Mo_2$, $Fe_{13}Ti_2Mo_1$, $Fe_{10}Mn_2Ti_2Mo_2$, $Fe_{13}Mn_1Mo_2$, $Fe_{13}Mn_1Ti_1Mo_1$, $Fe_{13}Mn_1Ti_2$, Fe_{16}, $Fe_{13}Mn_2Mo_1$, and $Fe_{13}Mn_2Ti_1$. Consequently, all solid solutions except $Fe_{13}Mn_2Mo_1$ and $Fe_{13}Mn_2Ti_1$ exhibit greater stability than Fe_{16}.

In subsequent analyses, we excluded the three solid solutions that are more difficult to form and less stable than Fe_{16}. Thus, mechanical properties and electronic structure analyses were conducted exclusively on the following six solid solutions: Fe_{16}, $Fe_{13}Ti_2Mo_1$, $Fe_{10}Mn_2Ti_2Mo_2$, $Fe_{13}Ti_1Mo_2$, $Fe_{13}Mn_1Ti_1Mo_1$, and $Fe_{13}Mn_1Ti_2$.

Orthogonal experimental range analysis was employed to evaluate the influence of *M* doping on the ductility (ε), formation enthalpy (H_{form}), and cohesive energy (E_{coh}) of $Fe_{16-x-y-z}Mn_xTi_yMo_z$. Using the data in Table 2, we calculated the index *W* and the range *R* according to Equation (4). Specifically, *W* represents the sum of the corresponding property values at *M* atomic percentages of 0, 6.25%, and 12.5%; *R* denotes the difference between the maximum and minimum values of the property across these doping levels. The magnitude of *R* reflects the extent to which *M* doping affects the respective property: a larger difference indicates a significant influence across doping levels, identifying the factor as primary; conversely, a smaller difference suggests limited impact, classifying it as secondary.

$$W = \sum Y_i, R = W_{max} - W_{min}, \quad (4)$$

In the equation, *i* denotes the atomic percentage of *M*; Y_i represents the values of ε, H_{form}, and E_{coh} corresponding to the atomic percentage of *M*; W_{max} is the maximum sum of the indicator values; and W_{min} is the minimum sum of the indicator values.

As shown in the orthogonal analysis results in Table 3, ε is most strongly influenced by Mo, followed by Ti, and least by Mn. This occurs because the large atomic

diameter difference between Fe and Mo induces significant lattice distortion, thereby exerting a dominant effect on ε upon doping. In contrast, the smaller atomic diameter differences between Fe-Ti and Fe-Mn result in minimal impact on ε during doping. Regarding H_{form}, Ti doping exerts the greatest influence, followed by Mn, with Mo showing the least effect. This indicates that Ti doping most effectively promotes solid solution formation, whereas Mo doping is least favorable for this process. For E_{coh}, Mo doping has the strongest influence, followed by Ti, and Mn exhibits the weakest effect. Consequently, Mo doping most significantly affects solid solution stability, while Mn doping has the least impact.

Table 3 Orthogonal test analysis of ε, H_{form} and E_{coh} of $Fe_{16-x-y-z}Mn_xTi_yMo_z$.

指标	ε/%			H_{form}/(kJ·mol^{-1})			E_{coh}/(kJ·mol^{-1})		
	Mn	Ti	Mo	Mn	Ti	Mo	Mn	Ti	Mo
K_0	13.22	8.85	6.1	–34.76	–17.46	–32.53	–1405.30	–1357.24	–1354.30
K_1	14.48	13.95	14.47	–31.25	–30.66	–31.50	–1384.78	–1383.60	–1385.04
K_2	14.53	19.43	21.39	–27.08	–44.97	–29.07	–1363.02	–1412.25	–1413.76
R	1.31	10.58	15.29	7.68	27.51	3.46	42.28	55.01	59.46
Ranking	Mo＞Ti＞Mn			Ti＞Mn＞Mo			Mo＞Ti＞Mn		

3.2 Density of States

The density of states reveals prominent features of the electronic structure[21]. Figure 2 presents the calculated total density of states (TDOS) and partial density of states (PDOS). The primary bonding peaks of the solid solution appear between -8.9 and 12.9 eV, arising from contributions of Fe 4s, Fe 3p, Fe 3d, Ti 4s, Ti 3p, Ti 3d, Mn 4s, Mn 3p, Mn 3d, Mo 4p, Mo 4d, and Mo 5s states. All alloy solid solutions exhibit no gap at the Fermi level, consistently demonstrating metallic character.

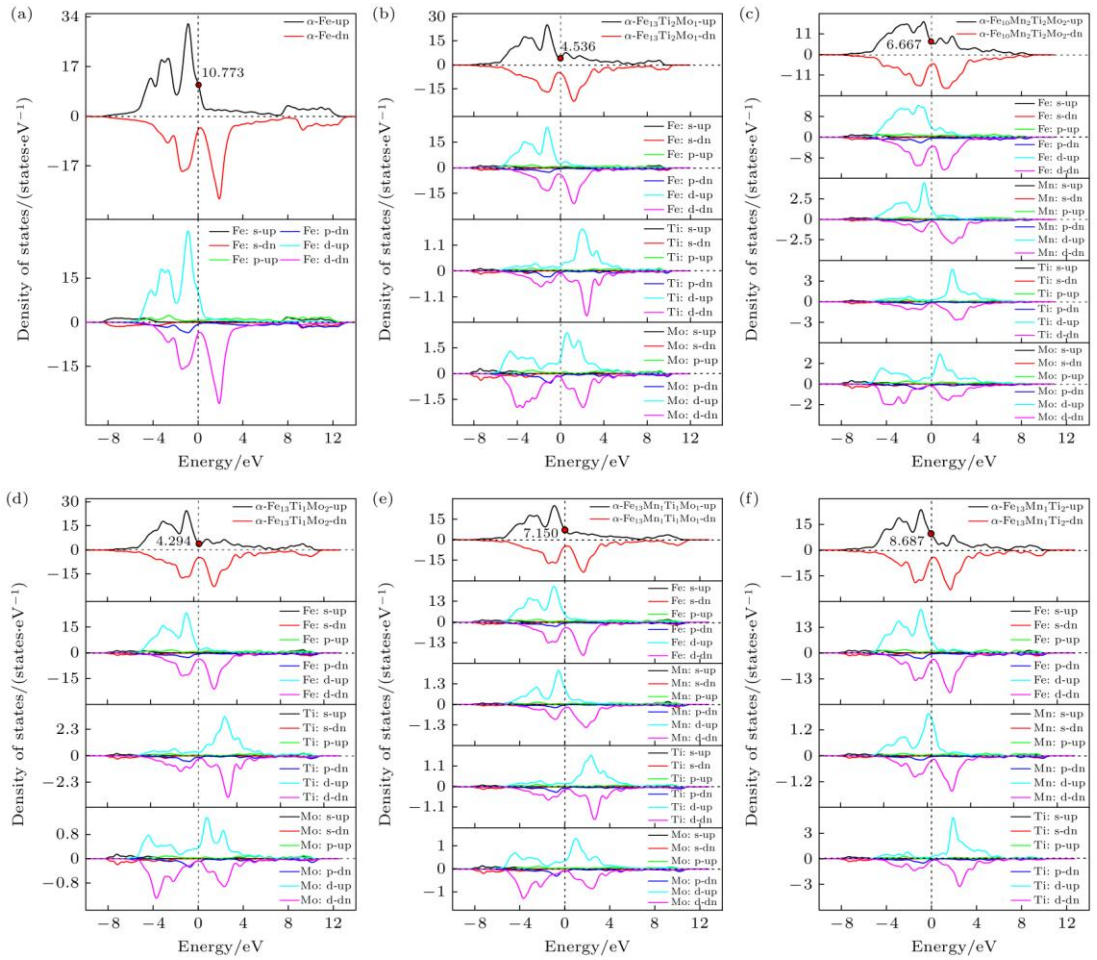

Fig. 2 Density of states and partial density of states plots: (a) Fe_{16}; (b) $Fe_{13}Ti_2Mo_1$; (c) $Fe_{10}Mn_2Ti_2Mo_2$; (d) $Fe_{13}Ti_1Mo_2$; (e) $Fe_{13}Mn_1Ti_1Mo_1$; (f) $Fe_{13}Mn_1Ti_2$.

As shown in Figure 2(a), the density of states (DOS) of Fe_{16} reveals that the energy range from -8.5 to -5.1 eV primarily arises from Fe 4s orbital contributions, whereas the range from -5.2 to 4.4 eV is dominated by Fe 4d orbitals. At the Fermi level, the DOS is mainly contributed by Fe 4d orbitals, reaching a high value of 10.773 states/eV. Compared with $Fe_{13}Ti_2Mo_1$, $Fe_{10}Mn_2Ti_2Mo_2$, $Fe_{13}Ti_1Mo_2$, $Fe_{13}Mn_1Ti_1Mo_1$, and $Fe_{13}Mn_1Ti_2$, the 3d states near the Fermi level are more densely distributed in Fe_{16}, indicating stronger electron localization and relatively lower stability.

Figure 2(b) displays the DOS of $Fe_{13}Ti_2Mo_1$. In the energy range from -5.6 to -1.9 eV, contributions primarily originate from Fe 3d, Ti 3d, and Mo 4d orbitals. The spin-up Ti 3d contribution is relatively weak, whereas spin-up Fe 3d and Mo 4d exhibit similar peaks, indicating orbital hybridization. Near the Fermi energy, the DOS is also dominated by Fe 3d, Ti 3d, and Mo 4d orbitals. In the range from 1.2 to 5.8 eV, these same orbitals contribute significantly; however, the spin-up Fe 3d contribution is reduced. Notably, spin-down Fe 3d, Ti 3d, and Mo 4d, along with spin-up Ti 3d and Mo 4d, display similar peaks, revealing pronounced hybridization and suggesting strong metallic or covalent bonding. The DOS at the Fermi level decreases to 4.536

states/eV, indicating that the introduction of Ti 3d and Mo 4d orbitals hybridizes with Fe 3d, leading to more delocalized electron distribution and enhanced stability.

As shown in Figure 2(c), the DOS of $Fe_{10}Mn_2Ti_2Mo_2$ indicates that the energy range from -5.5 to -1.7 eV is primarily contributed by Fe 3d, Mn 3d, and Mo 4d orbitals, with minor contributions from spin-down Fe 3p and Mn 3p. Spin-up Fe 3d, Mn 3d, and Mo 4d exhibit similar peaks, signifying hybridization. Near the Fermi energy, the DOS is dominated by Fe 3d, Mn 3d, and Mo 4d orbitals, with relatively weak contributions from Mo 4d and spin-up Mo 4p. In the range from 0 to 4.6 eV, Fe 3d, Mn 3d, Ti 3d, and Mo 4d orbitals contribute substantially. Spin-down Fe 3d, Mn 3d, Ti 3d, and Mo 4d, as well as spin-up Ti 3d and Mo 4d, show similar peaks, indicating strong hybridization and the presence of robust metallic or covalent bonds. Compared with $Fe_{13}Ti_2Mo_1$ and $Fe_{13}Ti_1Mo_2$, the co-doping of Mn 3d, Ti 3d, and Mo 4d induces hybridization; however, Mn doping increases the number of electrons in the 3d states, enhancing localization and consequently raising the DOS at the Fermi level to 6.677 states/eV.

Figure 2(d) presents the DOS of $Fe_{13}Ti_1Mo_2$. In the range from -5.5 to -1.6 eV, contributions mainly stem from Fe 3d, Ti 3d, and Mo 4d orbitals, with a relatively weak spin-up Ti 3d contribution. Fe 3d and Mo 4d exhibit similar peaks, indicating hybridization. Near the Fermi energy, the DOS is again dominated by Fe 3d, Ti 3d, and Mo 4d orbitals. In the range from 0.3 to 5.6 eV, these orbitals remain the primary contributors; however, the spin-up Fe 3d contribution is reduced. Spin-down Fe 3d, Ti 3d, and Mo 4d, along with spin-up Ti 3d and Mo 4d, display similar peaks, revealing significant hybridization and strong metallic or covalent bonding. The DOS at the Fermi level for $Fe_{13}Ti_1Mo_2$ is only 4.294 states/eV. Compared with $Fe_{13}Ti_2Mo_1$, the reduced Ti concentration and increased Mo concentration result in greater overlap between Fe 3d and Mo 4d peaks than between Fe 3d and Ti 3d, indicating stronger Fe 3d-Mo 4d hybridization. Consequently, the Fermi-level DOS of $Fe_{13}Ti_1Mo_2$ is lower than that of $Fe_{13}Ti_2Mo_1$, implying superior stability for $Fe_{13}Ti_1Mo_2$.

As shown in Figure 2(e), the DOS of $Fe_{13}Mn_1Ti_1Mo_1$ reveals that the energy range from -5.3 to -1.8 eV is primarily contributed by Fe 3d, Mn 3d, Ti 3d, and Mo 4d orbitals, with the spin-up Ti 3d contribution being the weakest. Fe 3d and Mn 3d exhibit similar peaks, indicating hybridization. Near the Fermi energy, the DOS is dominated by these same orbitals, though Ti 3d contributes relatively little. In the range from 0.2 to 5.0 eV, Fe 3d, Mn 3d, Ti 3d, and Mo 4d orbitals are the main contributors; however, spin-up Fe 3d and Mn 3d contributions are reduced. Spin-down Fe 3d, Mn 3d, Ti 3d, and Mo 4d, along with spin-up Ti 3d and Mo 4d, overlap significantly, demonstrating hybridization. Compared with $Fe_{10}Mn_2Ti_2Mo_2$, the DOS at the Fermi level increases to 7.150 states/eV. This rise results from reduced doping concentrations, which weaken the contributions of Mn 3d, Ti 3d, and Mo 4d,

decrease their overlap with Fe 3d orbitals, reduce hybridization, and thereby elevate the Fermi-level DOS.

Figure 2(f) shows the DOS of $Fe_{13}Mn_1Ti_2$. In the range from -5.8 to -1.6 eV, contributions primarily arise from Fe 3d, Mn 3d, and Ti 3d orbitals, with a relatively weak spin-up Ti 3d contribution. Spin-up Fe 3d and Mo 4d overlap, producing hybridization. Near the Fermi energy, the DOS is dominated by Fe 3d and Mn 3d orbitals, with Mn 3d contributing more significantly. In the range from 1.1 to 4.9 eV, Fe 3d, Ti 3d, and Mo 4d orbitals are the main contributors; spin-up Ti 3d contributes relatively strongly, while spin-down states are primarily from Fe 3d, Mn 3d, and Ti 3d, exhibiting similar peaks and clear hybridization. Near the Fermi level, Mn 3d doping supplies abundant electrons, and the highest spin-up Mn 3d peak nearly intersects the Fermi level, greatly enhancing electron localization and raising the DOS at the Fermi level to 8.687 states/eV.

According to the rigid-band theory, the magnitude of the DOS at the Fermi level serves as a criterion for phase stability: a lower DOS at the Fermi level corresponds to greater stability[22]. Comprehensive analysis shows that the total DOS at the Fermi level for the various solid solutions, ordered from lowest to highest, is $Fe_{13}Ti_1Mo_2$, $Fe_{13}Ti_2Mo_1$, $Fe_{10}Mn_2Ti_2Mo_2$, $Fe_{13}Mn_1Ti_1Mo_1$, $Fe_{13}Mn_1Ti_2$, and Fe_{16}. Consequently, their stability, from strongest to weakest, follows the same sequence: $Fe_{13}Ti_1Mo_2$, $Fe_{13}Ti_2Mo_1$, $Fe_{10}Mn_2Ti_2Mo_2$, $Fe_{13}Mn_1Ti_1Mo_1$, $Fe_{13}Mn_1Ti_2$, and Fe_{16}. Thus, stability assessments based on both DOS and binding energy yield consistent results.

3.3 Charge Difference Density

Figure 3 presents the planar charge difference density maps for Fe_{16}, $Fe_{13}Ti_2Mo_1$, $Fe_{10}Mn_2Ti_2Mo_2$, $Fe_{13}Ti_1Mo_2$, $Fe_{13}Mn_1Ti_1Mo_1$, and $Fe_{13}Mn_1Ti_2$. Charge difference density effectively reflects bonding behavior between adjacent atoms, with relative intensity indicated by color mapping[23]. For Fe_{16}, the absence of dopant atoms results in no discernible bonding features. In contrast, $Fe_{13}Ti_2Mo_1$, $Fe_{10}Mn_2Ti_2Mo_2$, and $Fe_{13}Ti_1Mo_2$ exhibit strong interatomic bonding, including Fe-Mn, Fe-Mo, Ti-Mo, and Mn-Ti metallic bonds as well as Fe-Ti ionic bonds. The charge difference density maps of $Fe_{13}Ti_2Mo_1$ and $Fe_{13}Ti_1Mo_2$ are similar; however, bonding in $Fe_{13}Ti_1Mo_2$ is more pronounced, as evidenced by deeper red and blue regions in Figure 3(d), indicating greater charge accumulation and depletion between atoms. The bonding in $Fe_{10}Mn_2Ti_2Mo_2$ is weaker than in $Fe_{13}Ti_2Mo_1$ and $Fe_{13}Ti_1Mo_2$, as shown by lighter red and blue hues in Figure 3(c), reflecting reduced charge transfer. This suggests that Mn doping diminishes binding strength, whereas Ti and Mo doping enhance it. Moreover, increasing Mo concentration while decreasing Ti concentration in $Fe_{13}Ti_1Mo_2$ relative to $Fe_{13}Ti_2Mo_1$ further strengthens bonding. The bonding in $Fe_{13}Mn_1Ti_1Mo_1$ is weaker than in $Fe_{10}Mn_2Ti_2Mo_2$, indicating that lower doping concentrations of Mn, Ti, and

Mo yield reduced binding strength. Finally, $Fe_{13}Mn_1Ti_2$ demonstrates that both Mn doping and increased Ti concentration are detrimental to enhancing binding strength.

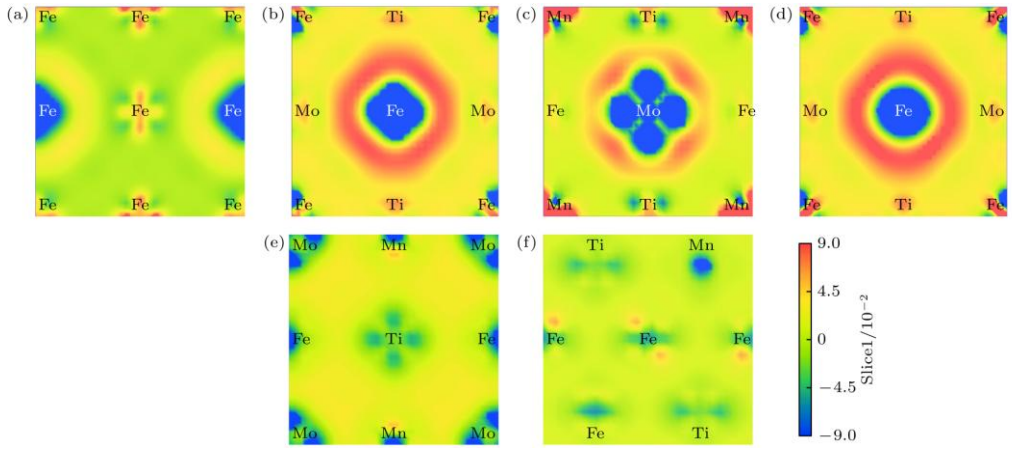

Fig. 3 Differential charge density diagram: (a) Fe_{16}; (b) $Fe_{13}Ti_2Mo_1$; (c) $Fe_{10}Mn_2Ti_2Mo_2$; (d) $Fe_{13}Ti_1Mo_2$; (e) $Fe_{13}Mn_1Ti_1Mo_1$; (f) $Fe_{13}Mn_1Ti_2$.

3.4 Mechanical Properties

Mechanical properties are characterized by elastic constants. These constants are physical parameters that describe a material's elastic mechanical behavior. They quantify the linear relationship between stress and strain within the elastic deformation regime and reflect the material's resistance to elastic deformation. For cubic crystal systems, mechanical stability requires the following conditions: $C_{11} > 0$, $C_{44} > 0$, $C_{11} - C_{12} > 0$, and $C_{11} + 2C_{12} > 0$. The calculated elastic constants and corresponding mechanical stability criteria for each solid solution are listed in Table 4. As shown, Fe_{16}, $Fe_{13}Ti_2Mo_1$, $Fe_{10}Mn_2Ti_2Mo_2$, $Fe_{13}Ti_1Mo_2$, $Fe_{13}Mn_1Ti_1Mo_1$, and $Fe_{13}Mn_1Ti_2$ all satisfy the mechanical stability conditions.

Table 4 Independent elastic constants and mechanical stability of $Fe_{16-x-y-z}Mn_xTi_yMo_z$.

试样	C_{11}	C_{12}	C_{44}	$C_{11}-C_{12}$	$C_{11}+2C_{12}$
Fe_{16}	296.273	159.033	126.763	137.240	614.339
$Fe_{13}Ti_2Mo_1$	292.506	158.281	117.403	134.225	609.068
$Fe_{10}Mn_2Ti_2Mo_2$	293.869	148.470	116.251	145.399	590.809
$Fe_{13}Ti_1Mo_2$	210.409	103.675	92.415	106.734	417.759
$Fe_{13}Mn_1Ti_1Mo_1$	291.402	158.680	123.704	132.722	608.762
$Fe_{13}Mn_1Ti_2$	275.790	150.536	112.712	125.254	576.862

The bulk modulus (B) and shear modulus (G) of solid solutions are commonly calculated using the Voigt-Reuss-Hill approximation, as expressed in Equations (5) and (6).

$$B_V = B_R = \frac{C_{11}+2C_{12}}{3},$$
$$G_V = \frac{C_{11}-C_{12}+3C_{44}}{5}, \quad (5)$$
$$G_R = \frac{5(C_{11}-C_{12})C_{44}}{4C_{44}+3(C_{11}-C_{12})},$$

$$B_H = \frac{B_V+B_R}{2}, G_H = \frac{G_V+G_R}{2}, \quad (6)$$

In the equation, the subscripts V, R, and H for *B* and *G* denote the Voigt, Reuss, and Voigt-Reuss-Hill approximation averages, respectively. The Voigt-Reuss-Hill approximation is defined as the arithmetic mean of the Voigt and Reuss approximations[24].

Using *B* and *G*, we calculated the Poisson's ratio (*v*), Young's modulus (*E*), the ratio (*K*) of shear modulus (G_H) to bulk modulus (B_H), and Vickers hardness (H_V) of the solid solution via Equation (7). The results are listed in Table 5.

Table 5 Mechanical property parameters of $Fe_{16-x-y-z}Mn_xTi_yMo_z$.

超胞	*B*/GPa			*G*/GPa			*E*/GPa	*K*	*v*	H_V
	B_V	B_R	B_H	G_V	G_R	G_H				
Fe_{16}	204.779	204.779	204.779	103.506	94.675	99.091	255.983	2.067	0.292	13.737
$Fe_{13}Ti_2Mo_1$	210.383	210.383	210.383	103.675	92.403	98.039	254.573	2.146	0.298	13.206
$Fe_{10}Mn_2Ti_2Mo_2$	196.401	196.401	196.401	98.830	91.632	95.231	245.942	2.062	0.291	13.272
$Fe_{13}Ti_1Mo_2$	202.961	202.961	202.961	97.287	90.163	93.725	243.667	2.165	0.300	12.496
$Fe_{13}Mn_1Ti_1Mo_1$	202.921	202.921	202.921	100.767	91.929	96.348	249.548	2.106	0.295	13.168
$Fe_{13}Mn_1Ti_2$	192.287	192.287	192.287	92.678	85.395	89.036	231.393	2.159	0.299	11.933

$$\begin{aligned} v &= \frac{3B_H-2G_H}{2(3B_H+G_H)}, E = \frac{9B_HG_H}{3B_H+G_H}, \\ K &= \frac{B_H}{G_H}, H_V = \frac{(1-2v)E}{6(1+v)}. \end{aligned} \quad (7)$$

Here, *E* reflects a material's resistance to tensile and compressive deformation. A higher *E* value indicates greater resistance. The descending order of *E* is Fe_{16}, $Fe_{13}Ti_2Mo_1$, $Fe_{13}Mn_1Ti_1Mo_1$, $Fe_{13}Mn_2Ti_2Mo_2$, $Fe_{13}Ti_1Mo_2$, $Fe_{13}Mn_1Ti_2$, indicating that *M* doping reduces the solid solution's resistance to tensile and compressive deformation.

Material brittleness and ductility can be assessed using *K* and *v*. When $K \geq 1.75$, the material exhibits ductility, with higher values indicating better ductility; otherwise, it behaves in a brittle manner, with lower values corresponding to greater brittleness[25]. Similarly, $v \geq 0.26$ signifies ductility, whereas values below this threshold indicate brittleness. A higher *v* implies superior ductility and enhanced resistance to brittle

fracture[26]. As shown in Table 5, both K and v follow the same descending sequence: $Fe_{13}Ti_1Mo_2$, $Fe_{13}Mn_1Ti_2$, $Fe_{13}Ti_2Mo_1$, $Fe_{13}Mn_1Ti_1Mo_1$, Fe_{16}, $Fe_{10}Mn_2Ti_2Mo_2$. All values exceed 1.75 and 0.26, respectively, confirming that all six solid solutions are ductile. Among them, $Fe_{13}Ti_1Mo_2$ demonstrates the best ductility, whereas $Fe_{10}Mn_2Ti_2Mo_2$ exhibits the poorest, thereby indicating that M doping enhances ductility. H_V characterizes a material's resistance to localized plastic deformation[27]. Table 5 further reveals that the Vickers hardness (H_V) of the six solid solutions decreases in the following order: Fe_{16}, $Fe_{10}Mn_2Ti_2Mo_2$, $Fe_{13}Ti_2Mo_1$, $Fe_{13}Mn_1Ti_1Mo_1$, $Fe_{13}Ti_1Mo_2$, $Fe_{13}Mn_1Ti_2$, confirming that M doping reduces solid solution hardness. The observed property variations stem primarily from atomic radius mismatches between M (Ti, Mn, Mo) and Fe. Doping induces lattice distortion, weakening direct Fe-Fe bonding and consequently lowering both tensile-compressive deformation resistance and hardness in $Fe_{16-x-y-z}Mn_xTi_yMo_z$ solid solutions[28]. However, lattice distortion enhances dislocation formation and mobility, facilitating deformation under external stress and thereby improving ductility. These findings offer valuable insights for designing tough, ductile ferrite-based steel materials[29].

4 Conclusions

1) H_{form} calculations indicate that all solid solutions form spontaneously. Ti doping most strongly promotes solid solution formation, followed by Mn, whereas Mo is least favorable. Among them, $Fe_{13}Ti_2Mo_1$ exhibits the lowest formation enthalpy and thus forms most readily.

2) E_{coh} results demonstrate that all solid solutions possess structural stability. Mo doping exerts the greatest influence on stability, followed by Ti, with Mn having the least effect. $Fe_{13}Ti_1Mo_2$ shows the largest absolute cohesive energy, indicating optimal structural stability.

3) Electronic structure analysis reveals increased overlap and pronounced hybridization between the 3d states of Mn and Ti, the 4d states of Mo, and the 3d states of Fe. This hybridization lowers the Fermi level, with $Fe_{13}Ti_1Mo_2$ exhibiting the lowest Fermi level and thus the highest stability.

4) Mechanical property calculations show that M doping reduces both tensile-compressive deformation resistance and hardness but enhances ductility. $Fe_{13}Ti_1Mo_2$ displays the best ductility, whereas $Fe_{13}Mn_1Ti_2$ exhibits the lowest hardness. These results provide a reference for designing tough, ductile ferrite-based steel materials.

Data Availability Statement

The data associated with this paper are available at Science Data Bank:

https://doi.org/10.57760/sciencedb.j00213.00227.

References

[1] Liu Q Y, Luo X, Zhu H Y, Han Y W, Liu J X 2017 *Acta Phys. Sin.* **66** 107501

[2] Yang Y X, Wang Z H, Wang Q, Tang C Y, Wan P, Cao D H, Dong C 2025 *Acta Phys. Sin.* **74** 058101

[3] Duan X G, Cai Q W, Wu H B 2011 *Acta Metall Sin.* **47** 251

[4] Zhu Y Y, Ning L K, Duan C H, Liu E Z, Tong J, Tan Z, Li H Y, Zhao L, Wang Z R, Zheng Z 2022 *Rare Metal Materials and Engineering.* **51** 1845

[5] Wang K, Xu H Y, Zheng X, Zhang H F 2025 *Acta Phys. Sin.* **74** 137101

[6] Qiu S H, Xiao Q Q, Tang H Z, Xie Q 2024 *Chin. J. Inorg. Chem.* **40** 2250

[7] Ding C, Wang C H, Zhang L L, Sun H B, Tian H B, Liu Q N 2025 *Chin. J. Rare Metals* **49** 389

[8] Ito K, Sawada H, Ogata S 2019 *Phys. Rev. Mater.* **3** 013609

[9] Zhang H, Sun M, Liu Y, Ma D, Xu B, Huang M X, Li D Z, Li Y 2021 *Acta Mater.* **211** 116878

[10] Uemori R, Chijiiwa R, Tamehiro H 1994 *Appl. Surf. Sci.* **76** 255

[11] Guo X, Zhou J T, Zhang X X, Yang P, Ren J Q, Lu X F 2022 *Comp. Mater. Sci.* **214** 111673

[12] Li K M, Schuler T, Fu C C, Nastar M 2024 *Acta Mater.* **281** 120355

[13] Neugebauer J, Hickel T 2013 *Wires Comput. Mol. Sci.* **3** 438

[14] Singh A, Wang J, Henkelman G, Li L 2024 *J. Chem. Theory Comput.* **20** 10022

[15] Forslund A, Jung J H, Srinivasan P, Grabowski B 2023 *Phys. Rev. B* **107** 174309

[16] Fedorov M, Wróbel J S, Fernández-Caballero A, Kurzydłowski K J, Nguyen-Manh D 2020 *Phys. Rev. B* **101** 174416

[17] Wang H Y, Hu Q K, Yang W P, Li X S 2025 *Acta Phys. Sin.* **74** 077101

[18] Błachowski A, Ruebenbauer K, Żukrowski J 2009 *J. Alloys Compd.* **482** 23

[19] Medvedeva N I, Park M S, Van Aken D C, Medvedeva J E 2014 *J. Alloys Compd.* **582** 475

[20] Hao P D, Chen P, Deng L, Li F X, Yi J H, Şopu D, Eckert J, Tao J M, Liu Y C, Bao R 2020 *J. Mater. Res. Technol.* **9** 3488

[21] Toriyama M Y, Ganose A M, Dylla M, Anand S, Park J, Brod M K, Munro J M, Persson K A, Jain A, Snyder G J 2022 *Mater. Today Electron.* **1** 100002

[22] Zhao W B, Guo E J, Zhang K, Tian X H, Tan C L 2021 *Scripta Mater.* **199**

113863
[23] Hu Y J, Shang S L, Wang Y, Darling K A, Butler B G, Kecskes L J, Liu Z K 2016 *J. Alloys Compd.* **671** 267
[24] Luo Y H 2022 *Materials* **15** 5656
[25] Nasir M T, Hadi M A, Rayhan M A, Ali M A, Hossain M M, Roknuzzaman M, Naqib S H, Islam A K M A, Uddin M M, Ostrikov K 2017 *Phys. Status Solidi (b)* **254** 1700336
[26] Li H, Wang Z J, Sun G D, Yu P F, Zhang W X 2016 *Solid State Commun.* **237** 24
[27] Ye D 2005 *Mater. Chem. Phys.* **93** 495
[28] Wang G, Schönecker S, Hertzman S, Hu Q M, Johansson B, Kwon S K, Vitos L 2015 *Phys. Rev. B* **91** 224203
[29] Lee C, Song G, Gao M C, Feng R, Chen P, Brechtl J, Chen Y, An K, Guo W, Poplawsky J D, Li S, Samaei A T, Chen W, Hu A, Choo H, Liaw P K 2018 *Acta Mater.* **160** 158